Journal of Materials Chemistry A

Accepted Manuscript

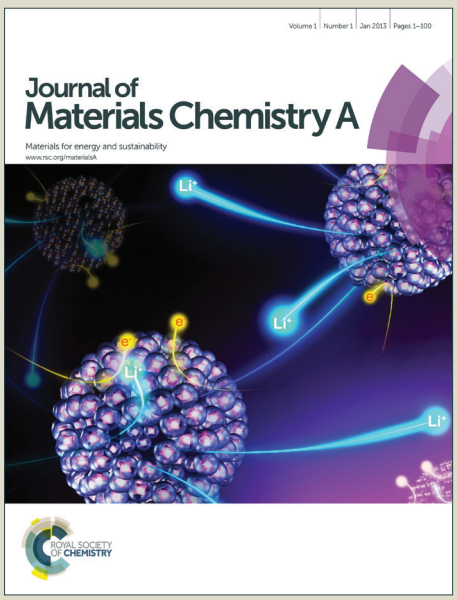

ROYAL SOCIETY OF CHEMISTRY

www.rsc.org/materialsA

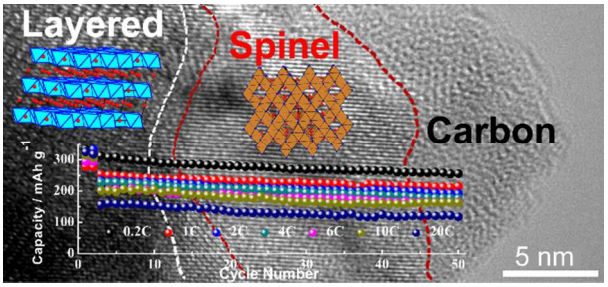

A Li-rich Layered@Spinel@Carbon heterostructured cathode material for LIBs, which comprises Li-rich layered core, a spinel interlayer and a carbon nano-coating.

A Li-Rich Layered@Spinel@Carbon Heterostructured Cathode Material for High Capacity and High Rate Lithium-Ion Batteries Fabricated *via* an *in situ* Synchronous Carbonization-Reduction Method

Qingbing Xia,[a] Xinfu Zhao,[a] Mingquan Xu,[a] Zhengping Ding,[a] Jiatu Liu,[a] Libao Chen,[a] Douglas G. Ivey[b] and Weifeng Wei*[a]

A novel Layered@Spinel@Carbon heterostructure is successfully fabricated *via* an *in situ* synchronous carbonization-reduction process based on a bio-inspired coating method, which comprises a core of Li-rich layered (R-3m) oxide, a spinel phase (Fd-3m) interlayer and a carbon nano-coating. This unique structure, which combines the advantages of the high capacity Li-rich layered structure, 3D fast Li^+ diffusion channels of the spinel structure and the high conductivity of the carbon coating, shows extremely high discharge capacity (as high as 334.5 mAh g^{-1}) and superior rate capability. This strategy may provide some new insights into the design and synthesis of various electrode materials for high performance energy storage devices.

Introduction

Lithium-ion batteries (LIBs), characteristic of higher energy density and much longer cycle life compared with other battery technologies, have been widely used as a key component in a variety of portable electronic devices. To meet increasing specific energy and power demands, particularly in the fields of electric tools, transportation and grid-scale energy storage, new Li-ion intercalated cathode materials possessing higher capacity and voltage are urgently needed.[1-7] Recently, Li-rich layered oxide materials, $x Li_2MnO_3 \bullet (1-x) LiMO_2$ (M refers to Mn, Ni, Co, *etc.*) have attracted intensive attention owing to their higher reported specific capacity

(more than 250 mAh/g), higher operating voltage and lower cost than other commercialized cathode materials, such as $LiCoO_2$, $LiFePO_4$ *etc*.[3, 8-10] However, Li-rich layered oxide materials still suffer from high 1st cycle irreversible capacity, limited cycle life and sluggish kinetics (*e.g.*, poor rate capability), which seriously hinder their practical applications.

The improvements pursued for Li-rich layered oxide materials are mainly focused on high rate capability, structural flexibility and stability related to cycle performance. Surface modification has been regarded as a promising strategy to enhance the electrochemical performance of Li-rich layered oxide materials. Coating materials, such as metal oxides,[11-14] fluorides and phosphates,[15-17] have been applied to stabilize the surface structure and to avoid side reactions with the electrolyte under high voltage and, in turn, to improve the cycle performance of Li-rich layered oxide materials. Other coating materials, such as Li^+-conducting materials $LiNiPO_4$ and Li_3VO_4,[18-20] have been employed to facilitate Li^+ migration, leading to enhanced rate capability and cycle performance. Unfortunately, these coating materials are generally not electronic conductors nor electrochemically active, resulting in limited performance improvement. Recently, spinel oxide cathode materials, which possess 3D Li^+ diffusion channels and high Li^+ diffusion coefficients,[21, 22] have been combined with layered oxides to fabricate layered/spinel heterostructure to improve the rate capability of Li-rich layered oxide cathode materials.[23-25] However, the spinel component shows inferior electronic conductivity and suffers from the Jahn-Teller effect which would deteriorate cycle performance.[21] In addition, the surface structure stability of layered/spinel heterostructure has not been significantly improved and still cannot avoid the problems of side reactions with the electrolyte under high voltage and metal ions dissolution during cycling. Hence, integration of high capacity Li-rich layered oxide materials with a hybrid coating layer, which has high Li^+ and electronic conductivity as well as electrochemical activity, would be an effective way to achieve high capacity and remarkable rate capability and enhanced cycle performance simultaneously.

Inspired by these considerations, we have developed a facile and controllable *in situ* synchronous carbonization-reduction route to fabricate a novel Layered@Spinel@Carbon heterostructured cathode material based on a bio-inspired coating method as illustrated in Scheme S1†. Dopamine, a biomolecule that can self-polymerize on virtually any surface in an alkaline solution,[26-28] was chosen as the carbon source. First, by depositing a uniform polydopamine layer onto the surface of a Li-rich layered oxide material, followed by subsequent carbonization, a carbon coated Li-rich layered oxide material is synthesized. During the carbonization process, a *in situ* layered-to-spinel phase transformation caused by carbothermal reduction takes place at the interface of Li-rich layered oxide materials and the carbon coating, forming a novel Layered@Spinel@Carbon (L@S@C) heterostructure, as shown in Scheme 1, with the following attributes: 1) The core region is the high capacity Li-rich layered oxide material; 2) the outermost layer is the carbon nanolayer which forms good electron transport pathways, acts as a protection layer that reduces the side reactions between electrode surface and the electrolyte, as well as increases the surface structural stability of the electrode, suppresses transition metal ions dissolution and reduces the HF attacks, thus improving the electronic conductivity and electrochemical performance; 3) the spinel interlayer possesses 3D Li^+ diffusion channels and acts as a Li^+ transfer accelerator to facilitate rapid Li^+ transport between the layered bulk and the electrolyte, which is beneficial to improve the rate capability. This unique Layered@Spinel@Carbon heterostructure combines the advantages of the Li-rich layered structure, the spinel structure and carbon, yields extremely high capacity, excellent cycle performance and superior rate capability.

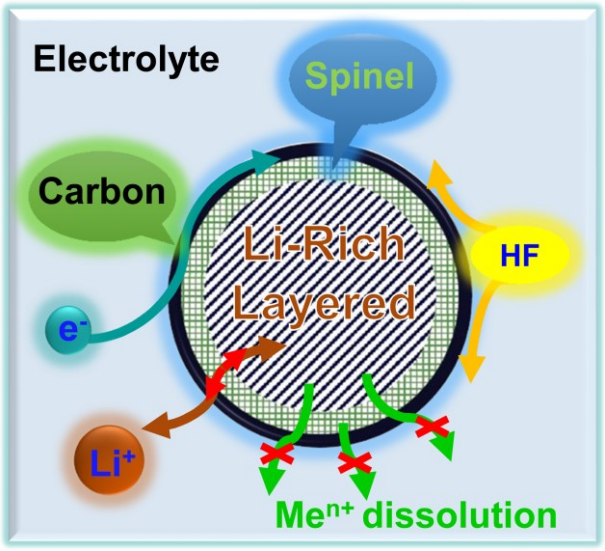

Scheme 1 Schematic view of the Layered@Spinel@Carbon heterostructure.

Experimental

Synthesis of the Li-rich layered oxide material

$0.33Li_2MnO_3 \cdot 0.67Li[Mn_{1/3}Ni_{1/3}Co_{1/3}]O_2$, was prepared using a co-precipitation method. $MnSO_4 \cdot H_2O$ (47.42 g), $NiSO_4 \cdot 6H_2O$ (29.65 g) and $CoSO_4 \cdot 7H_2O$ (31.39 g) with a stoichiometric ratio of 2.5:1:1 were dissolved in distilled water to form a 1 M mixed solution (500 mL). Then the mixed solution was separately pumped into a continuously stirred reactor under N_2 atmosphere at 60℃. At the same time, 2 M NaOH aqueous solution and an appropriate amount of 0.5 M ammonia solution were also separately fed into the reactor. During the co-precipitation process, the pH value was controlled at 11 by adjusting the pumping rate of ammonia solution. The as-precipitated product was filtrated, washed several times with distilled water and dried in a vacuum oven at 110℃ for 12 h. The obtained precursor was mixed with a stoichiometric amount of $LiOH \cdot H_2O$ (5% excess), calcined at 500℃ for 3h and then calcined at 850℃ in air at a heating rate of 1℃/min. The as-calcined product was named pristine.

Synthesis of the Layered@Spinel@Carbon heterostructured material (L@S@C)

200 mg pristine $0.33Li_2MnO_3 \bullet 0.67Li[Mn_{1/3}Ni_{1/3}Co_{1/3}]O_2$ and 60 mg dopamine were dispersed in 60 mL of 10 mM Tris-buffer aqueous solution (pH: ~ 8.5) and polymerized for 6 h under continuous stirring conditions. The polydopamine-coated pristine sample was carbonized at 550℃ for 10 min and then cooled to room temperature in air. The obtained composite was denoted as L@S@C-1. The effects of coating time and the concentration of dopamine were also compared in this work. For L@S@C-2, the polymerization time was prolonged to 12 h, yet keeping other reaction conditions fixed (initial dopamine concentration was 1 mg/mL). L@S@C-3 was synthesized similarly to L@S@C-1, but the initial dopamine concentration was raised to 2 mg/mL.

Materials characterization

The structure of the as-prepared oxides and composites were characterized by X-ray diffraction (XRD) (Rigaku D/Max-2500 Diffractometer with Cu Kα radiation) and selected area electron diffraction (SAED) with a field-emission JEOL JEM-2100F transmission electron microscope (TEM). The morphology was evaluated using a Nova Nano SEM230 field emission scanning electron microscope (SEM) and a JEOL JEM-2100F TEM. Chemical state and composition analysis were carried out by X-ray photoelectron spectroscopy (XPS) using an ESCALAB 250Xi X-ray photoelectron spectrometer. Etching with Ar^+ ions was used to determine depth profiles of Mn, Ni and Co. The etching rate was estimated as 5.4 nm min^{-1}. All XPS spectra were corrected using the C1s line at 284.8 eV. Curve fitting and background subtraction were accomplished using Thermo Avantage version 5.52.

Electrochemical testing

The synthesized oxides and composites were mixed with acetylene black and polyvinylidene fluoride in a weight ratio of 8:1:1 in N-methyl-2-pyrrolidone to form a slurry. Subsequently, the slurry was coated onto Al foil and then dried at 110℃ for 12 h in a vacuum oven to obtain as-prepared cathodes. The electrochemical testing was conducted with CR2025 coin-type

half-cells assembled in an Ar-filled glove box. The half-cells consisted of an as-prepared cathode, a Li metal anode, a Celgard 2500 separator and 1 M $LiPF_6$ in EC-DMC (weight ratio 1:1) electrolyte solution. The cells were cycled on a battery testing system (LANHE CT2001A, Wuhan LAND electronics Co., P. R. China) between 2.0 and 4.8 V at different rates.

Results and Discussion

Morphology and Structure Characterizations

Fig. 1 shows the scanning electron microscopy (SEM) images of the pristine and heterostructured samples. It is clearly shown that both the pristine and heterostructured samples are consisted of numerous nanoplates with smooth surface. After carbon coating treatment, for the heterostructure, the morphology is hardly changed (Fig. 1b-d). Structural information for as-prepared pristine and heterostructured samples was identified using powder X-ray diffraction (XRD) as shown in Fig. 2. The main reflections for all the samples can be indexed as a layered α-$NaFeO_2$ structural type with R-3m symmetry, except for some weak superstructure reflections around 20 to 25°. These reflections are ascribed to Li/Mn cation ordering in the transition metal layer of the monoclinic (C2/m) Li_2MnO_3 region.[8, 29] It should be noted, however, that no reflections corresponding to carbon were observed in the XRD patterns, presumably due to its low mass loading. Compared with the pristine sample, the main reflections for the heterostructured samples become broader and satellite humps appear next to each main reflection. When the polymerization time was prolonged (L@S@C-2) or the initial dopamine concentration was increased (L@S@C-3), the humps become even broader, especially in the L@S@C-3 sample, which are clearly revealed by the magnified XRD patterns on the right. These satellite humps can be assigned to the X-ray reflections for the spinel structure (Fd-3m),[24, 30-32] suggesting that a layered-to-spinel structural transformation occurred during the carbonization process. Varying the polymerization time or

the initial concentration of dopamine, results in the variation of carbon content, and the formation of the spinel structure is believed to associate with the pyrolytic carbon.

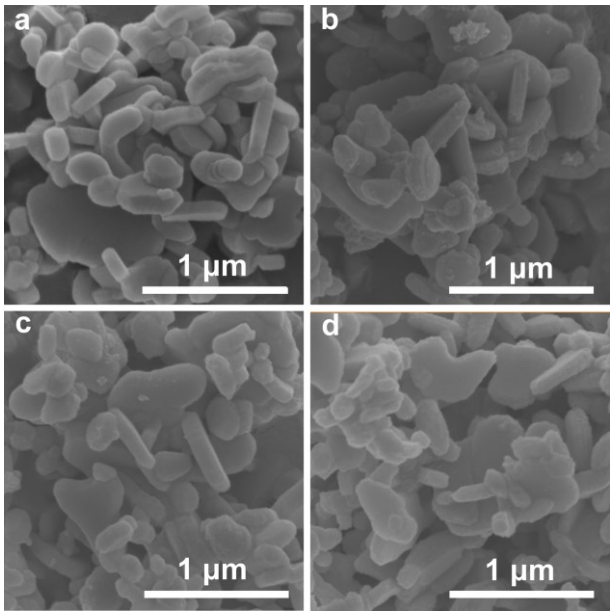

Fig. 1 SEM images of pristine and heterostructured samples. (a) Pristine; (b) L@S@C-1; (c) L@S@C-2; (d) L@S@C-3;

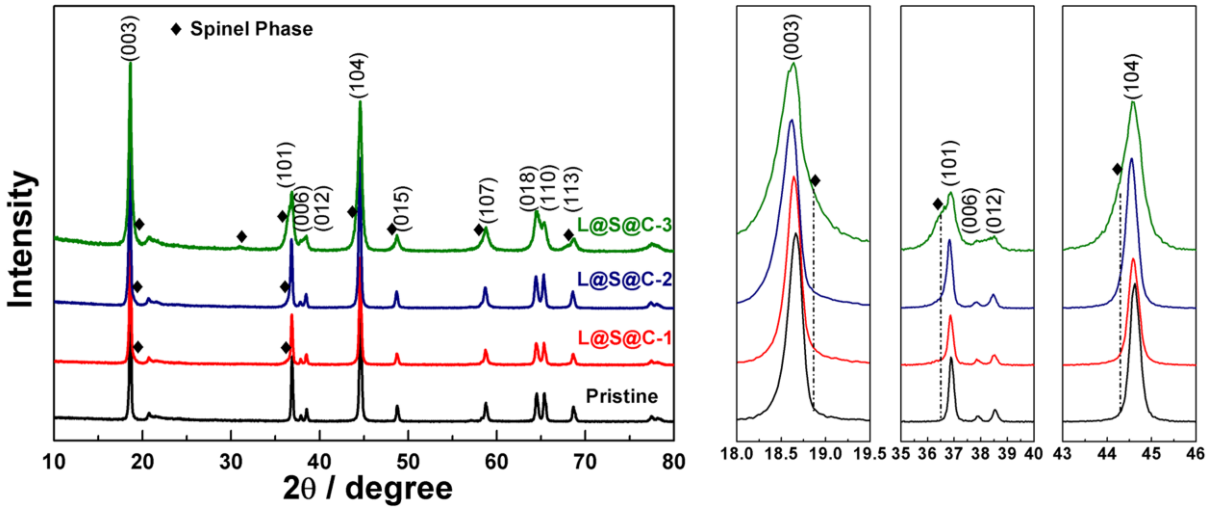

Fig. 2 Powder XRD patterns for pristine and heterostructured samples.

To further confirm the structural transformation and spinel phase formed during the carbonization process, the pristine and heterostructured samples were observed using transmission electron microscopy (TEM). It is apparent (Fig. 3a and d) that the primary particles of pristine and heterostructured samples are well-defined nanoplates with a thickness

around 100 to 200 nm. A high resolution TEM (HRTEM) micrograph (Fig. 3b) taken from the pristine sample exhibits two sets of lattice fringes, rotated by 60°, with the same interplanar spacing (0.242 nm); these correspond to the (010) and (100) planes of the layered structure. The corresponding selected area electron diffraction (SAED) pattern in Fig. 3c reveals hexagonal symmetry, which is typical for a R-3m space group along the [001] zone axis. For the polycrystalline electron diffraction rings (Fig. 3e) taken from the heterostructured sample, there are three diffraction rings inconsistent with any planes of the layered structure (R-3m). These three diffraction rings can be indexed to the (220), (422) and (442) planes of the spinel phase (Fd-3m), indicative of the formation of a new layered/spinel heterostructure (Fig. 3e and f). From the HRTEM image in Fig. 3g, it is noted that this distinct heterostructure consists of three different layers, forming a novel Layered@Spinel@Carbon heterostructure as vividly illustrated in Fig. 3h. The outermost layer is a carbon nano-coating with a thickness of ~6 nm generated from the pyrolysis of polydopamine. L@S@C-2 and L@S@C-3 were prepared by varying the coating time and initial dopamine concentration, respectively, for the two samples, the carbon coating are around 7 nm and 16 nm in thickness (Fig. S1†). This indicates that the thickness of the carbon coating can be tailored through varying the initial concentration of dopamine or the polymerization time.[26, 33] As shown in the enlarged image (Fig. 3i), the inner part shows a typical layered structure with two interplanar spacings of 0.475 nm and 0.244 nm corresponding to (003) and (101) planes of the layered structure, respectively. The interlayer presents another type of structure and the lattice spacings of 0.209 nm and 0.146 nm are consistent with the interplanar spacings of (400) and (440) planes of the cubic spinel structure (Fig. 3j). The corresponding fast Fourier transformation (FFT) pattern (Fig. 3k) shows four fold symmetry and further confirms its spinel nature. The spinel phase formed at the interface of Li-rich layered bulk and the carbon coating, suggesting that the formation of spinel phase is most likely to be induced by the carbothermal reduction during the carbonization process under high temperature. Between the layered and the spinel areas,

there exists a narrow transition area that integrates both the layered and spinel regions (Fig. 3g). This indicates that the layered structure forms good structural compatibility with the newly formed spinel phase since the oxygen arrangement of cubic spinel structure and hexagonal layered structure are both cubic close packing.[34] It should be noted that the newly formed spinel phase has 3D Li^+ diffusion channels, higher electronic conductivity and Li^+ diffusion coefficient than that of the Li-rich layered bulk. Therefore, such two-phase fused area would provide an efficient path for Li^+ and electron conduction. Consequently, it can be surmised that a small portion of the layered structure was gradually transformed into the spinel structure through *in situ* synchronous carbonization-reduction process, forming a new heterostructure that consists of a high capacity Li-rich layered oxide core, a spinel interlayer with fast 3D Li^+ diffusion channels and a highly conductive carbon layer.

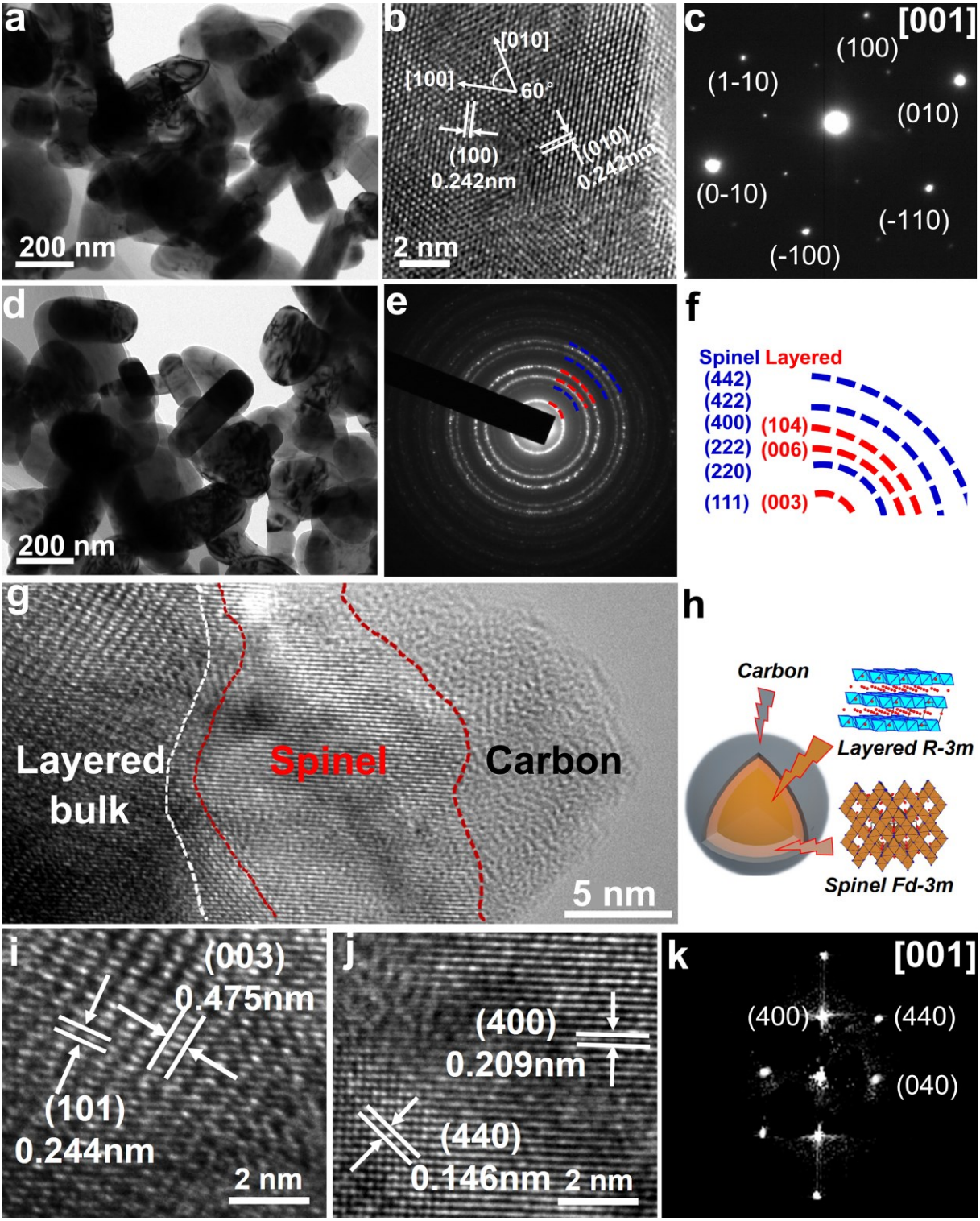

Fig. 3 TEM bright filed image (a) and HRTEM image (b) of pristine sample. (c) Corresponding SAED pattern of (b) along the [001] zone axis. (d) TEM bright filed image of L@S@C-1 sample. Polycrystalline SAED pattern (e) and index of the diffraction rings (f) corresponding to the region in (d). (g) HRTEM image of L@S@C-1 sample. (h) Schematic

view of the heterostructure. (i) and (j) Detailed HRTEM images of the layered and spinel areas. (k) Corresponding FFT patterns for image (j).

X-ray photoelectron spectroscopy (XPS) measurements were employed to investigate the variation in chemical states and composition. Fig. 4a shows typical XPS spectra for Ni2p, Co2p and Mn2p for the pristine and heterostructured samples. In the pristine sample, the observed binding energies of 855.08, 780.28 and 642.58 eV coincide well with those for Ni^{2+}, Co^{3+} and Mn^{4+}, respectively.[14, 18] After carbonization, the binding energies for the Ni2p and Co2p spectra of the heterostructured sample were retained, while the peaks of Mn2p3/2 and Mn2p1/2 slightly shift toward lower binding energies, suggesting a lower oxidation state than tetravalent for Mn appeared.[35, 36] The variation in Mn oxidation can be reasonably attributed to the effect of carbothermal reduction, due to the highly reducibility of carbon under high temperature. The XPS depth profiles for the pristine and heterostructured samples are compared in Fig. 4b. It is apparent that the atomic ratios of Mn, Ni and Co barely change in the pristine sample, which is consistent with the nominal composition. However, depletion of Mn and Ni was detected in the sub-surface regions (as marked by the dotted box) in the heterostructured sample, suggesting that substantial ion rearrangement occurred during the carbonization process. During the heat treatment process, the polydopamine coating converted into carbon, forming a Layered@Carbon intermediate transition structure. Meanwhile, the tetravalent Mn ions on the surface areas along the carbon coating were reduced to a lower oxidation state with the assistance of pyrolytic carbon simultaneously. The metal ions rearranged to maintain the balance of valence state accompanied with the variation in transition metal ratio, leading to the *in situ* layered-to-spinel structural transformation and formation of the Layered@Spinel@Carbon heterostructure. Note that the layered (R-3m) structure and cubic (Fd-3m) spinel structure have the same oxygen arrangement, only differing in the position of the transition metal ions and Lithium ions. For the Li-rich layered structure $(Li)_{3a}[Li_xM_{1-x}]_{3b}O_2$, the transition metal ions locate in 3b octahedron sites, Lithium

ions occupy the 3a tetrahedron sites and a small portion of Lithium ions locate in 3b octahedron sites in the transition metal layer.[29] During the metal ions rearrangement process, part of the transition metal ions migrate from the 3b into the 16d octahedron sites and the Lithium ions move into the 8a tetrahedron sites, forming the cubic spinel structure $(Li)_{8a}[M_2]_{16d}O_4$ (Fig. S2†).[21]

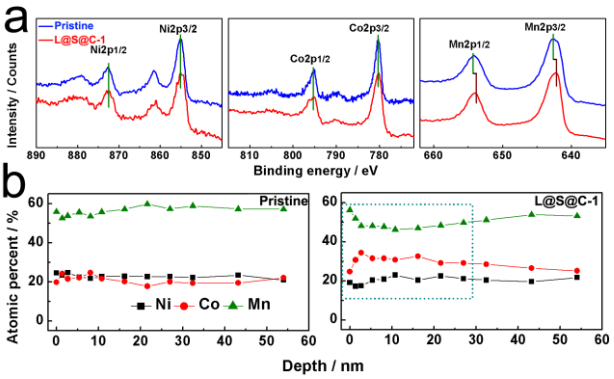

Fig. 4 (a) XPS spectra for Ni2p, Co2p and Mn2p for the pristine and L@S@C-1 samples. (b) Compositional variation for the transition metals as function of etched depth.

Electrochemical Performance

Typical initial charge and discharge curves for the pristine and heterostructured samples, taken at 0.1 C (25 mA/g) rate between 2.0 and 4.8 V, are shown in Fig. 5a. During the charging process, both samples exhibit two distinguishable stages, a smoothly sloping voltage profile below 4.5 V corresponding to Li^+ deintercalation from the $LiMn_{1/3}Ni_{1/3}Co_{1/3}O_2$ component and a long plateau around 4.5 V related to Li and O extracted from the Li_2MnO_3 phase and structural rearrangement.[37, 38] Compared with the pristine sample, a discharging plateau around 2.7 V appeared in all heterostructured samples, which is the characteristic of the spinel structure.[15, 23, 31] Furthermore, the corresponding dQ/dV cures (Fig. 5b) clearly show a cathodic peak at around 2.8 V, which refers to the Li^+ intercalation/deintercalation mechanism of the newly formed spinel structure component in the heterostructured samples, suggesting that the spinel interlayer also participates in the electrochemical reaction in the first charge/discharge process. The initial charge/discharge capacities and coulombic

efficiency of the pristine and heterostructured samples are tabulated in Table 1. L@S@C-1 delivers a maximal discharge capacity of 334.5 mAh/g that is the highest ever reported for Li-rich layered oxides (Table S1†),[10-12, 14, 15, 17, 18, 23, 24] while the pristine sample only yields 290.2 mAh/g. In addition, the heterostructure also significantly improve the coulombic efficiency, the L@S@C-1 sample achieves a coulombic efficiency as high as 92.2%. As the coating time or the concentration of dopamine increases (*e.g.*, L@S@C-2 and L@S@C-3), the charge plateau around 4.5 V become shorter and the ~2.7 V discharge plateau longer, resulting a decreased charge capacity but improved discharge capacity and coulombic efficiency. These results imply that a portion of Li_2MnO_3 phase was pre-activated with the assisted of carbothermal reduction. During the discharge process, the Li^+ can intercalate into the newly formed spinel phase around 2.7 V, leading to higher discharge capacities. Meanwhile, the carbon nano-coating can improve the surface structural stability of the electrode, thus reducing the structural rearrangement during charging process. Hence, the enhanced discharge capacity and coulombic efficiency observed in the heterostructured L@S@C-1 sample could be reasonably attributed to synergic effects arising from the carbothermal-induced electrochemical activity spinel interlayer and the stabilization of the electrode surface structure. However, a significant amount of the layered structure transforms into the spinel phase which delivers lower charge capacity than the pristine $0.33Li_2MnO_3 \bullet 0.67Li[Mn_{1/3}Ni_{1/3}Co_{1/3}]O_2$, resulting in a corresponding deterioration in the discharge capacity and coulombic efficiency (L@S@C-3).

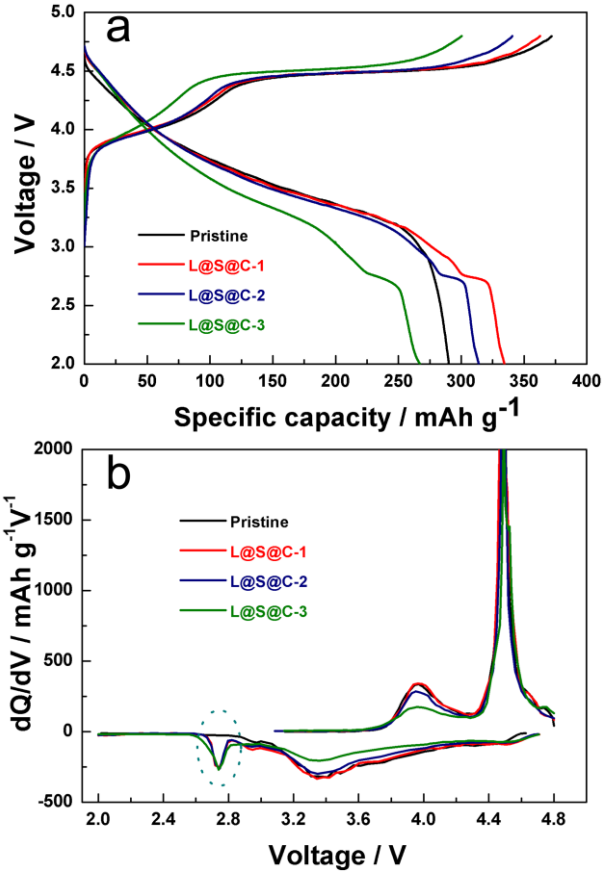

Fig. 5 (a) Typical initial charge-discharge curves. (b) Corresponding dQ/dV curves of the pristine and heterostructured samples.

Table 1 The first charge and discharge capacities and corresponding coulombic efficiency of the pristine and heterostructured samples cycled between 2.0 V and 4.8 V at 0.1 C (25 mA/g).

	Charge capacity (mAh g^{-1})	Discharge capacity (mAh g^{-1})	Coulombic efficiency (%)
Pristine	372.1	290.2	78
L@S@C-1	362.9	334.5	92.2
L@S@C-2	343.3	314	91.5
L@S@C-3	300.6	267.2	88.9

The cycle performance of the pristine and heterostructured samples was evaluated at 0.2 C between 2.0 and 4.8 V after an initial 0.1 C activation cycle. As shown in Fig. 6a (and Fig. S3†), L@S@C-1 and L@S@C-2 deliver higher discharge capacity than the pristine sample. After 60 cycles, the L@S@C-1 sample exhibits a discharge capacity of 250.4 mAh/g,

whereas the pristine sample decays to 187.7 mAh/g. However, both the pristine and the heterostructure samples undergo an inevitable layered-to-spinel phase transformation (Fig. S4†) during the deep cycling.[39, 40] It should be note that, for the heterostructure, the carbothermal-induced spinel interlayer has stable 3D framework and achieves better structural compatibility with the layered cores, which can increase the structural stability and restrain further structural transformation.[23, 41] Furthermore, the outmost carbon layer can also stabilize the surface structure of electrode, reduce side reactions between electrode surface and the electrolyte, protect the active materials from HF attacks and avoid the metal ions dissolution. Therefore, the synergic effects of the carbon nano-coating layer and the well structural compatibility between the layered bulk and spinel interlayer contribute to the improved cycle performance.

To investigate the discharge rate capability, the cells were charged galvanostatically to 4.8 V at 0.1 C and then discharged at various rates from 1 C to 30 C, as shown in Fig. 6b-d (and Fig. S5†). The heterostructured samples maintain the discharge plateau at around 2.7 V, which is related to the spinel structure with high Li^+ conductivity. The plateau is maintained even at a 10 C discharge rate, suggesting good structural stability between the spinel interlayer and layered cores. The corresponding discharge capacities (Table S2†) are generally higher than that of the pristine sample and the capacity differences become more remarkable with increasing discharge rate. When discharged at 2 C, the L@S@C-1 sample delivered a higher discharge capacity of 273.2 mAh/g, whereas the pristine sample showed a lower capacity of 187.4 mAh/g. After 50 cycles, more than 200 mAh/g is retained for the L@S@C-1 sample, but the pristine sample suffers from continuous structural transformation, inferior electronic conductivity and surface damage, decays to 130 mAh/g. By increasing the discharge rate to 10 C, more surprisingly, the L@S@C-1 sample exhibited a discharge capacity of 233.7 mAh/g, which is approximate 3.2 times that of the pristine sample. Even for ultra-high discharge rates of 20 C and 30 C, the L@S@C-1 sample can still yield discharge

capacities of 162.4 mAh/g and 122.7 mAh/g, which are much higher than 98.5 mAh/g and 55.3 mAh/g, respectively, for the pristine sample.

In order to systematically evaluate the rate properties of the pristine and heterostructured samples, electrochemical cycles under high charge/discharge rates were also carried out in this work. As shown in Fig. 6e and f, at 1 C charge and discharge rate, the discharge capacity of the heterostructured L@S@C-1 sample maintains 214.7 mAh/g after 50 cycles, which is significantly higher than that of the pristine sample (155 mAh/g). As the charge and discharge rate increase from 2 C to 20 C, the heterostructured samples exhibit superior rate performance compared with the pristine sample (Fig. S6†). It is noted that the discharge capacity of the L@S@C-1 sample obtained at 10 C is even higher than that of pristine cycled at 1 C. At 20 C charge and discharge rates, nearly no discharge capacity was observed for the pristine sample, while the L@S@C-1 sample achieved a reversible discharge capacity of more than 120 mAh/g. The poor rate performance of pristine could originate from the increasing charge-transfer resistance caused by side reactions with the electrolyte and the intrinsic sluggish kinetics, which limits Li^+ transport between the bulk and the electrolyte. For the heterostructure, the carbothermal-induced spinel interlayer has 3D Li^+ diffusion channels that can greatly shorten the Li^+ diffusion distance and facilitate Li^+ intercalation/deintercalation processes. In addition, the conductive carbon nanolayer forms an electrical network between adjacent particles and current collectors, which can significantly enhance electronic conductivity and effectively reduce the overall polarization. Therefore, the superior rate performance of the heterostructure can be reasonably attributed to both the carbothermal-induced spinel phase and the outmost carbon nanolayer.

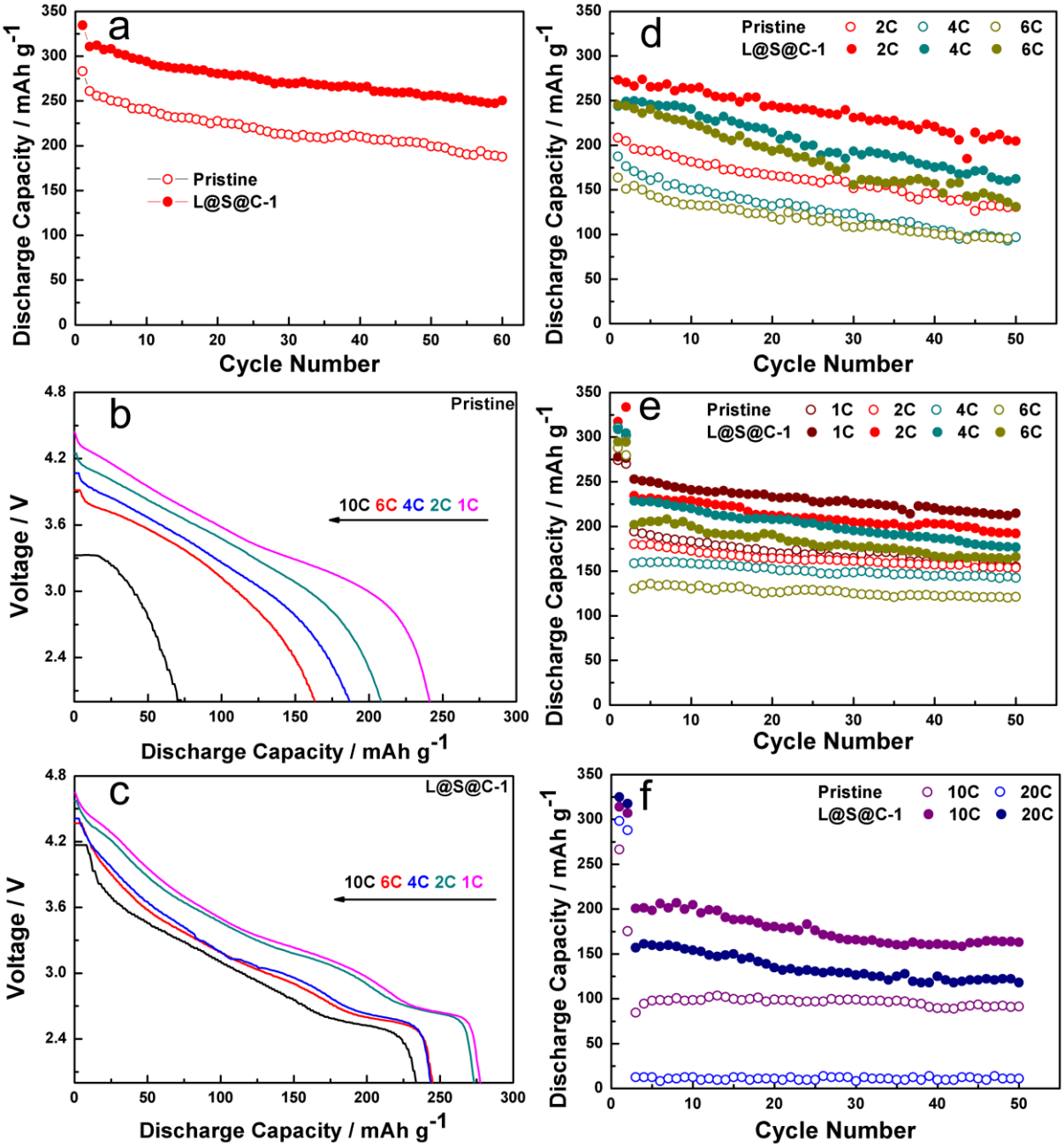

Fig. 6 (a) Cycling performance of the pristine and L@S@C-1 samples at 0.2 C. (b) and (c) Discharge voltage profiles of pristine and L@S@C-1 samples at different rates (0.1 C charge rate). (d) Cycling performance of pristine and L@S@C-1 samples at different rates (0.1 C charge rate). (e) and (f) Charge/discharge rate performance after two activation cycles at 0.1 C rate.

Conclusion

A novel Layered@Spinel@Carbon heterostructured cathode material utilized in LIBs was successfully synthesized *via* a carbothermal reduction route. A spinel phase *in situ* forms along the layered bulk/carbon interface with the assistance of carbon reduction, which expedites Li^+ intercalation/deintercalation between electrolyte and Li-rich layered cores. In addition, the carbon nanolayer acts as a fast electron conduction path, effectively suppresses side reactions with the electrolyte and stabilizes the surface structure of electrode. This well-designed heterostructure takes full advantage of high capacity Li-rich layered cores, the spinel interlayer with high Li^+ conductivity and the conductive carbon nanolayer to obtain extremely high capacity and superior rate capability. It is anticipated that the current experimental findings may provide some technical insights to further improve the capacity and rate capability of lithium ion positive materials, paving the path for the next-generation high performance LIBs.

Acknowledgements

This work was funded by the Recruitment Program of Global Youth Experts, the National Natural Science Foundation of China (51304248), the Program for New Century Excellent Talents in University (NCET-11-0525) and the Program for Shenghua Overseas Talents from Central South University (CSU).

Notes and references

[a] State Key Laboratory of Powder Metallurgy, Central South University, Changsha, 410083, P. R. China.

[b] Department of Chemical and Materials Engineering, University of Alberta, Edmonton, AB T6G 2V4, Canada.

* To whom correspondence should be addressed. E-mail: weifengwei@csu.edu.cn; Fax/Tel: +86 73188877876.

† Electronic Supplementary Information (ESI) available: Additional electrochemical data. See DOI: 10.1039/c000000x/.

1. M. Armand and J. M. Tarascon, *Nature*, 2008, **451**, 652.
2. B. Dunn, H. Kamath and J. M. Tarascon, *Science*, 2011, **334**, 928.
3. M. M. Thackeray, C. Wolverton and E. D. Isaacs, *Energy Environ. Sci.* , 2012, **5**, 7854.
4. H.-C. Yu, C. Ling, J. Bhattacharya, J. Thomas, K. Thornton and A. Van der Ven, *Energy Environ. Sci.* , 2014, **7**, 1760.
5. Y.-G. Guo, J.-S. Hu and L.-J. Wan, *Adv. Mater.* , 2008, **20**, 2878.
6. X. Meng, X.-Q. Yang and X. Sun, *Adv. Mater.* , 2012, **24**, 3589.
7. C. Yuan, H. B. Wu, Y. Xie and X. W. Lou, *Angew. Chem. Int. Ed.* , 2014, **53**, 1488.
8. M. M. Thackeray, S.-H. Kang, C. S. Johnson, J. T. Vaughey, R. Benedek and S. Hackney, *J. Mater. Chem.* , 2007, **17**, 3112.
9. N. S. Choi, Z. Chen, S. A. Freunberger, X. Ji, Y. K. Sun, K. Amine, G. Yushin, L. F. Nazar, J. Cho and P. G. Bruce, *Angew. Chem. Int. Ed.* , 2012, **51**, 9994.
10. H. Yu and H. Zhou, *J. Phys. Chem.Lett.*, 2013, **4**, 1268.
11. S. Guo, H. Yu, P. Liu, X. Liu, M. Chen, M. Ishida and H. Zhou, *J. Mater. Chem. A*, 2014, **2**, 4422.
12. F. Wu, N. Li, Y. Su, H. Lu, L. Zhang, R. An, Z. Wang, L. Bao and S. Chen, *J. Mater. Chem.* , 2012, **22**, 1489.
13. Y. Wu and A. Manthiram, *Solid State Ionics* 2009, **180**, 50.
14. X. Zhang, I. Belharouak, L. Li, Y. Lei, J. W. Elam, A. Nie, X. Chen, R. S. Yassar and R. L. Axelbaum, *Adv. Energy Mater.*, 2013, **3**, 1299.
15. Y.-K. Sun, M. J. Lee, C. S. Yoon, J. Hassoun, K. Amine and B. Scrosati, *Adv. Mater.* , 2012, **24**, 1192.
16. M.-S. Park, J.-W. Lee, W. Choi, D. Im, S.-G. Doo and K.-S. Park, *J. Mater. Chem.* , 2010, **20**, 7208.

17. Q. Wang, J. Liu, A. V. Murugan and A. Manthiram, *J. Mater. Chem.* , 2009, **19**, 4965.

18. Q. Fu, F. Du, X. Bian, Y. Wang, X. Yan, Y. Zhang, K. Zhu, G. Chen, C. Wang and Y. Wei, *J. Mater. Chem. A*, 2014, **2**, 7555.

19. D. Shin, C. Wolverton, J. Croy, M. Balasubramanian, S. H. Kang, C. L. Rivera and M. M. Thackeray, *J. Electrochem. Soc.* , 2011, **159**, A121.

20. S.-H. Kang and M. M. Thackeray, *Electrochem. Commun.* , 2009, **11**, 748.

21. A. Kraytsberg and Y. Ein-Eli, *Adv. Energy Mater.*, 2012, **2**, 922.

22. A. Manthiram, K. Chemelewski and E.-S. Lee, *Energy Environ. Sci.* , 2014, **7**, 1339.

23. F. Wu, N. Li, Y. Su, H. Shou, L. Bao, W. Yang, L. Zhang, R. An and S. Chen, *Adv. Mater.* , 2013, **25**, 3722.

24. D. Wang, I. Belharouak, G. Zhou and K. Amine, *Adv. Funct. Mater.* , 2013, **23**, 1070.

25. D. Luo, G. Li, C. Fu, J. Zheng, J. Fan, Q. Li and L. Li, *Adv. Energy Mater.*, DOI: 10.1002/aenm.201400062.

26. R. Liu, S. M. Mahurin, C. Li, R. R. Unocic, J. C. Idrobo, H. Gao, S. J. Pennycook and S. Dai, *Angew. Chem. Int. Ed.* , 2011, **50**, 6799.

27. H. Lee, S. M. Dellatore, W. M. Miller and P. B. Messersmith, *Science*, 2007, **318**, 426.

28. A. Postma, Y. Yan, Y. Wang, A. N. Zelikin, E. Tjipto and F. Caruso, *Chem. Mater.* , 2009, **21**, 3042.

29. A. R. Armstrong, M. Holzapfel, P. Novák, C. S. Johnson, S.-H. Kang, M. M. Thackeray and P. G. Bruce, *J. Am. Chem. Soc.* , 2006, **128**, 8694.

30. I. Belharouak, G. M. Koenig Jr, J. Ma, D. Wang and K. Amine, *Electrochem. Commun.* , 2011, **13**, 232.

31. D. Kim, G. Sandi, J. R. Croy, K. G. Gallagher, S.-H. Kang, E. Lee, M. D. Slater, C. S. Johnson and M. M. Thackeray, *J. Electrochem. Soc.* , 2013, **160**, A31.

32. L. Zhou, D. Zhao and X. Lou, *Angewandte Chemie-International Edition*, 2012, **51**, 239.

33. H. Jiang, L. Yang, C. Li, C. Yan, P. S. Lee and J. Ma, *Energy Environ. Sci.* , 2011, **4**, 1813.

34. M. M. Thackeray, C. S. Johnson, J. T. Vaughey, N. Li and S. A. Hackney, *J. Mater. Chem.* , 2005, **15**, 2257.

35. Y.-K. Sun, S. T. Myung, M. H. Kim, J. Prakash and K. Amine, *J. Am. Chem. Soc.* , 2005, **127**, 13411.

36. A. Abouimrane, O. C. Compton, H. Deng, I. Belharouak, D. A. Dikin, S. T. Nguyen and K. Amine, *Electrochem. Solid-State Lett.* , 2011, **14**, A126.

37. N. Yabuuchi, K. Yoshii, S.-T. Myung, I. Nakai and S. Komaba, *J. Am. Chem. Soc.* , 2011, **133**, 4404.

38. S. Hy, F. Felix, J. Rick, W.-N. Su and B. J. Hwang, *J. Am. Chem. Soc.* , 2014, **136**, 999.

39. J. Zheng, M. Gu, A. Genc, J. Xiao, P. Xu, X. Chen, Z. Zhu, W. Zhao, L. Pullan, C. Wang and J.-G. Zhang, *Nano Lett.* , 2014, **14**, 2628.

40. M. Gu, I. Belharouak, J. Zheng, H. Wu, J. Xiao, A. Genc, K. Amine, S. Thevuthasan, D. R. Baer and J.-G. Zhang, *ACS Nano*, 2012, **7**, 760.

41. Y. Cho, S. Lee, Y. Lee, T. Hong and J. Cho, *Adv. Energy Mater.*, 2011, **1**, 821.